Research Article

Nano Research
2024, 17(6): 5138–5147

ISSN 1998-0124 CN 11-5974/O4
https://doi.org/10.1007/s12274-024-6429-4

Low-temperature-pyrolysis preparation of nanostructured graphite towards rapid potassium storage with high initial Coulombic efficiency

Jingke Ren[1,§], Boyu Xing[1,§], Wen Luo[2] (✉), Binyang Luo[1], Xinfei Wu[1], Xin Yan[2], Wencong Feng[1], Feiyue Wang[1], Chaojie Cheng[1], and Liqiang Mai[1] (✉)

[1] *State Key Laboratory of Advanced Technology for Materials Synthesis and Processing, Wuhan University of Technology, Wuhan 430070, China*
[2] *Department of Physics, School of Science, Wuhan University of Technology, Wuhan 430070, China*
[§] *Jingke Ren and Boyu Xing contributed equally to this work.*

Received: 7 November 2023 / **Revised:** 18 December 2023 / **Accepted:** 19 December 2023

ABSTRACT

Industrially prepared artificial graphite (AG) is attractive for potassium-ion batteries (PIBs), but its rate performance is poor and the production process is energy intensive, so developing an efficient strategy to produce novel graphite with low energy consumption and high performance is economically important. Herein, a nanostructured graphite composed of multi-walled carbon nanotubes (MWCNTs) and graphite shells was prepared by one-pot method through low-temperature pyrolysis of iron-based metal-organic framework (MOF) and carbon source. The high graphitization degree of nanostructured graphite makes the initial Coulombic efficiency (ICE) exceed 80%, and the three-dimensional (3D) conductive network ensures a specific capacity of 234 mAh·g^{-1} after 1000 cycles at a high current density of 500 mA·g^{-1}. In addition, the typical graphite potassium storage mechanism is also demonstrated by *in situ* X-ray diffraction (XRD) and *in situ* Raman spectroscopy, and its practicality is also proved by the voltage of the full cells. This work provides a feasible way to optimize the practical production process of AG and expand its application in energy storage.

KEYWORDS

graphite anode, potassium-ion batteries, high graphitization degree, low-temperature pyrolysis, initial Coulombic efficiency

1 Introduction

The rechargeable battery market has been dominated by lithium-ion batteries (LIBs) since their commercialization in 1991, but the scarcity of lithium resource has made them increasingly expensive [1–4]. At the same time, the vigorously developed new energy sources such as wind and solar energy, generally have intermittent characteristics, making them unable to be directly connected to the grid for use [5]. Fortunately, large-scale electric energy storage systems (EESs) can effectively solve the intermittent problem of new energy sources mentioned above by shaving peaks and filling valleys on the power grid [6]. Therefore, with the development of new energy, it has become an urgent task to find a safe, reliable, and cost-effective energy storage technology for the construction of large-scale EESs. Compared with lithium, sodium, and potassium in the same main group are abundant in nature, so the raw materials of sodium and potassium elements are much cheaper [7, 8]. Hence, using Na^+ and K^+ as substitutes for Li^+ in energy storage field is currently a research hotspot.

Potassium-ion batteries (PIBs) have obvious advantages over sodium-ion batteries (SIBs) in many aspects. The redox potential of the Na^+/Na (−2.72 V vs. standard hydrogen electrode (SHE)) is higher than that of the K^+/K (−2.93 V vs. SHE), indicating a higher working voltage of full cells and thereby a higher energy density [9, 10]. In terms of anode materials, Na/graphite cells can only form a NaC_{64} binary intercalation compound, providing a theoretical capacity about 35 mAh·g^{-1} unless expanded graphite is used or solvent molecules are co-inserted. In contrast, K^+ can be matched to the graphite anode used in LIBs and forms a KC_8 binary intercalation compound, providing a theoretical capacity about 279 mAh·g^{-1} [11–13]. In addition, the K^+ intercalation/deintercalation plateau in graphite is long and stable above 0.1 V versus K^+/K. This suitable voltage can avoid potassium dendrites and reduce the probability of short circuit [14–20]. It also can provide high energy density by high working voltage when matched with suitable cathode. For example, the average discharge voltages of ~ 3.58 and ~ 3.5 V were exhibited by $K_2Mn[Fe(CN)]_6$||graphite and $K_{1.75}Mn[Fe(CN)_6]_{0.93}\cdot 0.16H_2O$||graphite which were demonstrated by Deng et al. [21] and Bie et al. [22] respectively. Therefore, the practicability of PIBs is promising to be achieved by the employment of graphite anode [23]. Generally, graphite materials with high chemical stability and conductivity, are widely used as the anode materials of LIBs. According to the report of Starting Point Research Institute (SPIR), the shipment of 2023H1 anode materials in China reached 708,000 tons, an increase of 38.6% year-on-year, of which natural graphite accounted for 14.4% and artificial graphite (AG) accounted for 84.1% [24]. Compared with natural graphite, AG is commonly used as a graphite electrode due to its high purity, and

Address correspondence to Wen Luo, luowen_1991@whut.edu.cn; Liqiang Mai, mlq518@whut.edu.cn

it is expected to be used in large-scale EESs due to its high yield and reversible potassium storage capacity. Unfortunately, the large radius of K^+ will lead to the huge volume expansion (~ 60%) and slow diffusion kinetics, thus further cause the structure degradation and fast capacity fading [25]. Therefore, to develop a novel graphite adapted to K^+ is necessary for the large-scale application of PIBs. More importantly, industrial production of AG requires high temperature, usually higher than 2800 °C, which will consume substantial energy and resource [26]. Hence, to explore a low energy consumption preparation technique to produce novel graphite with appropriate properties has a good application prospect in the field of large-scale EESs. In short, using the existing AG production line to produce graphite anode compatible with PIBs and significantly reduce the manufacturing cost can promote the application of PIBs for large-scale EESs.

Low-dimensional nano-graphite is one of the important members of graphitic materials [27–32]. Neuromorphic graphitic carbon has been designed by Lu et al. via simultaneously sintering iron citrate and multi-walled carbon nanotubes (MWCNTs) to improve the graphitic anode of PIBs, but its initial Coulombic efficiency (ICE) is lower than 35%, and the raw material (MWCNTs) are expensive [28]. Similarly, a highly graphitized carbon nanofiber membrane was developed by Xing et al. via heating the polyacrylonitrile fibrous membrane for advanced PIBs, but it is not economical because its low yield and the high synthesis temperature of 2800 °C [29]. Herein, a nanostructured graphite composed of MWCNTs and graphite shells was synthesized by one-pot method through low-temperature sintering of MIL-100 (Fe) and glucose (GLC) at 1100 °C. This was done for two reasons: (i) metal-organic framework (MOF) materials are capable to accommodate many molecules with a large internal space and adjustable pore size [33], making them ideal carriers for graphitizing carbon sources. (ii) Carbon atoms can diffuse into the metal alloy and then precipitate and crystallize during sintering, and the crystallization energy barrier of carbon atoms can be reduced thus reducing the graphitization temperature. Among the many metal catalysts, iron has the highest catalytic activity, followed by cobalt, and then nickel, which can be proved by the interplanar spacing of the (002) crystal plane and Raman intensity ratio between D and G peaks of the obtained graphitic carbon [34]. Consequently, we developed a low-temperature pyrolysis preparation of nanostructured graphite by simultaneously sintering GLC and MIL-100 (Fe). When this nanostructured graphite is used as an anode for PIBs, its high graphitization degree allows the ICE to exceed 80%, much higher than the reported literatures [27, 35–37]. The unique three-dimensional (3D) structure can effectively improve the electronic conductivity and alleviate the volume expansion, thus reducing the polarization and improving the rate performance of graphite potassium storage. It still delivers a specific capacity of 234 $mAh \cdot g^{-1}$ at a current density of 500 $mA \cdot g^{-1}$ after 1000 cycles. Moreover, the low potential platform of nanostructured graphite makes it has the advantage of assembling high voltage full cells.

2 Experimental section

2.1 Chemicals and materials

The 1,3,5-benzenetricarboxylic acid and 1,2-dimethoxyethane (DME) were 98% and 99.5% pure brought from Aladdin. The AG was mesophase carbon microsphere graphite brought from Shenzhen Kejing Star. The perylene-3,4,9,10-tetracarboxylic dianhydride (PTCDA) was 98% pure brought from Macklin. The potassium bis(fluoroslufonyl)imide (KFSI) was 99.8% pure brought from DoDoChem. All other used reagents in this work were analytical grade and obtained from HUSHI (Shanghai, China).

2.2 Material synthesis

MIL-100 (Fe) was prepared by hydrothermal synthesis. Specifically, a total of 1.8 g of 1,3,5-benzenetricarboxylic acid, 720 mg of iron powder, 60 mL of H_2O, 1000 μL of HNO_3, and 1000 μL of HF were mixed evenly at the same time [38]. The obtained mixture was placed in a high-pressure autoclave and heated at 150 °C for 12 h to yield orange precipitates. After centrifugation and washing by H_2O to remove unreacted residual ions, the orange powders were obtained. The MIL-100 (Fe) was stored for use after being dried in air at 90 °C.

The graphitic carbon materials were obtained by simultaneously sintering a series of mixtures of MIL-100 (Fe) and GLC with different mass ratios. Specifically, fine powder mixture composed of MIL-100 (Fe) and GLC was obtained by grinding. The obtained powder was firstly pre-sintered at 1100 °C for 6 h in Ar with the heating rate of 10 $°C \cdot min^{-1}$. Then the resultant carbon was calcined at 450 °C for 12 h in air with the heating rate of 10 $°C \cdot min^{-1}$. After iron components were removed by the hydrochloric acid of 2 M and the hydrochloric acid had been washed away, a series of graphitic carbon materials were finally obtained after drying.

2.3 Material characterization

The *ex situ* and *in situ* X-ray diffraction (XRD) tests were performed on Bruker D2 and Bruker D8 X-ray diffractometer respectively with Cu Kα radiation (λ = 1.5406 Å). The *ex situ* and *in situ* Raman spectra tests were performed on the HORIBA HR Evolution spectroscopy equipment with lasers wavelength of 532 and 633 nm respectively. The thermogravimetric (TG) tests were performed by the Netzsch STA 449F3 thermal analysis instrument. The scanning electron microscopy (SEM) tests were performed by the JEOL-7100F microscopy. The transmission electron microscopy (TEM) test, the high-resolution TEM (HRTEM) test, and the high-angle annular dark field scanning TEM (HAADF-STEM) test were carried out using the JEM-2100F and Titan G260-300 electron microscopy equipment. The surface areas tests using Brunauer–Emmett–Teller (BET) method were achieved by the Tristar II 3020 instrument.

2.4 Electrochemical measurements

The CR2016 coin cells were assembled in an Ar atmosphere glove box. The electrodes of graphitic active materials were papered by the active materials and carboxymethyl cellulose (CMC) sodium at a mass ratio of 9:1. The Cu foil was used as current collector and finally punched to an electrode in a diameter of 10 mm with a mass loading of 1–1.5 $mg \cdot cm^{-2}$. The cathode of the full cells was made of PTCDA, conductive agent (Ketjen black), and CMC binder in a mass ratio of 6:3:1. The Al foil was used as current collector and finally punched to an electrode in a diameter of 10 mm with a mass loading of 1.2–1.9 $mg \cdot cm^{-2}$. K foil was used as the counter electrode of half cells, and the glass microfiber filter was used as the separator (Whatman, Grade GF/D). The electrolyte was self-made and the 3 M KFSI in DME solution was used in both half cells and full cells. The tests of cycling performance, rate performance, and the galvanostatic intermittent titration technique (GITT) tests were all carried out at potential window of 0.01 to 3 V on the LAND CT2001A battery testing instruments. The tests of cyclic voltammetry (CV) and electrochemical impedance spectroscopy (EIS) in the frequency range from 0.01 Hz to 100 kHz were taken by CHI600E electrochemical workstation. All electrochemical tests were carried out at room temperature.

3 Results and discussion

MIL-100 (Fe) has an open internal space with a maximum aperture of 29 angstroms, its synthesis process is simple and does not involve organic solvent [38, 39], the details of the synthesis and its related characterizations are displayed in the experimental section and Electronic Supplementary Material (ESM; Fig. S1 in the ESM). MIL-100 (Fe) was mixed with GLC and the obtained mixture was heated by two steps in tube furnace, the first was pre-sintering at 1100 °C in an inert atmosphere to obtain nanostructured graphite and the second step was calcining at 450 °C in air to remove amorphous carbon [25]. The graphitization degree of the products at different mass radio of MIL-100 (Fe) to GLC was investigated, and different nanostructured graphitic carbon materials were achieved (Scheme 1). After removing iron with 2 M hydrochloric acid, the final products were obtained. The pristine graphite shells were synthesized when no GLC was added; a composite of graphite shells and hollow nanoparticles was achieved when 1.5 times the mass of GLC was added; in contrast, a composite of MWCNTs and graphite shells was obtained when 2.0 times the mass of GLC was added. The products of the different sintering stages were denoted as P-MOF and P-MOF-A for pure MIL-100 (Fe) pre-sintering at 1100 °C in inert atmosphere and further calcining at 450 °C in the air respectively. As displayed from Figs. 1(a) and 1(b), the XRD test result of the P-MOF has a distinct amorphous carbon peak, which is manifested as a broad (002) crystal plane diffraction peak [40]; moreover, its Raman spectroscopy test result also shows a high D peak, confirming the presence of amorphous carbon [41]. Whereas, after further calcination in air, the amorphous carbon in the P-MOF is removed, leaving only the graphite component [42]. The P-MOF and P-MOF-A are further explored by TG test after removing iron, the results are shown in Fig. 1(c). Clearly, the graphite component begins to react in air at 510 °C, and the proportion of amorphous carbon in the pre-sintered product is close to 10 wt.%. Therefore, it can be assumed that the pyrolysis of MIL-100 (Fe) alone cannot yield highly graphitized carbon materials. In other words, it can be inferred that the introduction of GLC can make the internal space of MIL-100 (Fe) be fully utilized to increase the graphitization degree of products. The amorphous carbon of about 10 wt.% will significantly reduce ICE. The two products, P-MOF and P-MOF-A, were assembled as the anode materials into half cells of PIBs under the same conditions for ICE test. It is obvious in Fig. 1(d) that the ICE is increased by 34.7% after removing the amorphous carbon by calcination in the air. To some extent, it can be considered that increasing the degree of graphitization is also improving ICE.

The catalytic ability of MIL-100 (Fe) for GLC was probed by gradient experiments with different mass ratios of GLC addition. It is suspected that the inability of pure MIL-100 (Fe) to form highly graphitic carbon is due to its large internal space, which makes itself unable to provide sufficient carbon source. Therefore, GLC was used as a carbon source supplement to improve the graphitization degree of sintered products [34]. The products of raw materials with different ratios in two sintering stages were investigated through a series of TG tests (Fig. S2 in the ESM). When the mass ratio of MIL-100 (Fe) to GLC is 1 wt.%:0.5 wt.% (Fig. S2(a) in the ESM), the amorphous carbon content of the product pre-sintered at 1100 °C is significantly lower than that without GLC, but still higher than 6%, indicating that the addition of GLC can improve the degree of graphitization of the product compare with pure MOF. Besides, it can be found from the TG results that further increasing the mass ratio will further reduce the content of amorphous carbon (Figs. S2(b)–S2(e) in the ESM), and maintain it at a low value eventually. However, when the mass ratio reaches 1:3.0, the pyrolysis product at 1100 °C manifested greatly expansion compared to other collapsed products of different mass ratios, which implied that the excess amount mixture of GLC would fail to be encapsulated into MIL-100 (Fe) (Fig. S3 in the ESM).

Moreover, the graphitization degree of the graphitic carbon materials obtained by pre-sintering was studied and compared with AG. As shown in Fig. 1(e), when the XRD half peak width of AG was set to 1.00, the half peak widths of the graphitic carbon materials obtained at the mass ratios of 1:1.0 and 1:2.0 were relatively small both around 1.50, which implied the achieved products exhibited good crystalline properties. However, the XRD pattern of the sample with mass ratio 1:1.0 still manifest some amorphous feature signals around 2θ of 17°–28° [43]. Therefore, the sample with mass ratio 1:2.0 displays the best crystalline properties among above samples. In order to quantitatively compare the graphitization degree of the graphitic carbons, Sadezky et al.'s method was used to fit and analyze the Raman spectra [44]. According to the above method, the D peak is divided into four parts, the D_1 (~ 1350 cm^{-1}) and D_2 (~ 1620 cm^{-1}) peaks are assigned to the lattice vibration modes of graphite with A_{1g} and E_{2g} symmetry, respectively. The D_3 (~ 1500 cm^{-1}) peak is derived from the amorphous carbon, the D_4 (~ 1200 cm^{-1}) peak is related to the sp^2–sp^3 bond vibration of the polyene-like structure. From Fig. 1(f), it is obvious that the integrated intensity ratio of the peak D_1 and the peak G (I_{D_1}/I_G) is the smallest at a mass ratio of 1:2.0, with a value of 0.49 closest to the AG value of 0.38. The $2D_1$ band is an overtone of the D_1 band, and is strongly influenced

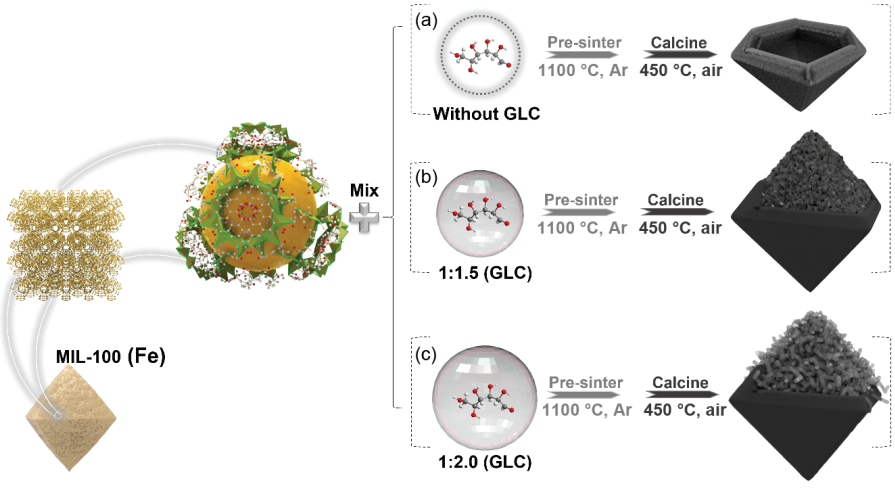

Scheme 1 Schematic diagram of the controllable synthesis of different nanostructured graphitic carbon materials. Mass ratio of MIL-100 (Fe) to GLC: (a) 1 wt.%: 0 wt.%, (b) 1 wt.%:1.5 wt.%, and (c) 1 wt.%:2.0 wt.%.

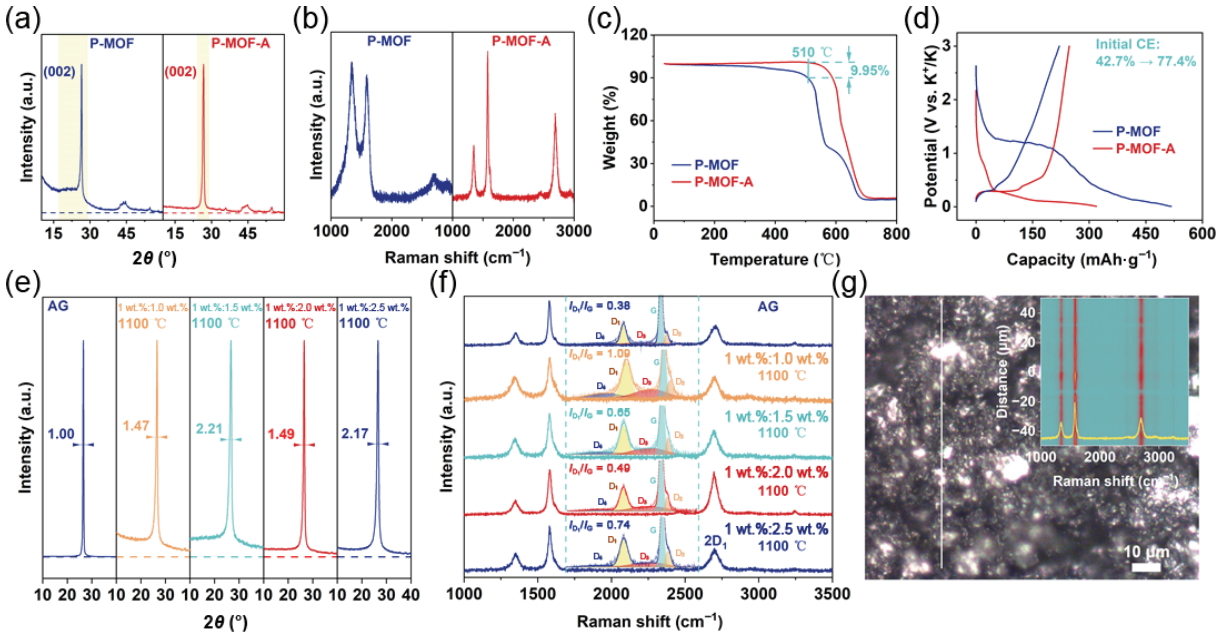

Figure 1 (a) XRD image, (b) Raman spectra image, and (c) TG results of P-MOF and P-MOF-A. (d) ICE results of P-MOF and P-MOF-A. (e) XRD patterns and (f) Raman spectra image of AG and graphitic carbon materials obtained by pre-sintering at different mass ratio. (g) Raman spectra line scan image of the graphitic carbon material obtained at the optimal mass ratio (insert: Raman spectroscopy signal intensity map on the line scanning path).

by the stacking level of the graphene layers [45, 46]. The $2D_1$ peak is strongest when the mass ratio is 1:2.0, which indicates that a relatively thicker graphene layer was grown in the *c*-axis direction of the graphite lattice. Its D_3 peak intensity is weak which also represents the least amount of amorphous carbon except AG. Moreover, the XRD and Raman spectra of the post-calcined products obtained at 450 °C in air under different mass ratios were shown in the ESM (Figs. S4 and S5 in the ESM) respectively. it can be expected that the half peak width of the mass ratio of 1:2.0 is still the narrowest, while the I_{D_1}/I_G and D_3 peak intensity are both the smallest. The above results indicate that the mass ratio of MIL-100 (Fe) to GLC is 1:2.0 exhibits the highest graphitization degree.

The effect of GLC was further explored by SEM and TEM, only graphite shells can be seen in the final product of pyrolyzed pure MIL-100 (Fe) (Fig. S6 in the ESM and illustrated in Scheme 1(a)), and when the mass ratio reached 1:1.5, the complex composed of graphite shells and hollow nanoparticles was achieved (Fig. S7 in the ESM and illustrated in Scheme 1(b)). The obtained graphitic carbon material of mass ratio about 1:2.0 was further characterized to study its morphological structure and composition. The Raman spectra line scan testing on the sample was conducted firstly, and the result are shown in Fig. 1(g). Comparing the two optical images of the achieved graphitic carbon material and AG (Fig. S8 in the ESM), the same metallic luster can be seen on their surfaces, indicating that the sample has the typical π bond of graphite which can reflect the natural light [47]. But the particle size of sample is much smaller than AG which implies that its structure has been nano-sized. Herein, the obtained nano-structured graphite with high graphitization degree was abbreviated as Nano-G. Moreover, the intensity of Raman peaks of Nano-G along the line-scanning path retains consistently, indicating the uniformity and highly graphitization features.

Figure 2(a) shows the SEM image of Nano-G, from which the closely linked large amounts of nanowires and relatively fewer bulks can be seen. TEM further reveals that the morphology of nanowires is essentially carbon nanotubes (Fig. 2(b)), and the bulks in SEM image are actual graphite shells (Fig. 2(c) and illustrated in Scheme 1(c)). Based on the similar shape of the graphite shells and MIL-100 (Fe) particle, it can be concluded that the graphite shells and carbon nanotubes were derived from the surface and the internal space of MIL-100 (Fe) particle respectively. HRTEM further confirmed that the nanowires are actual MWCNTs with a typical graphite interlayer spacing of 0.343 nm (Fig. 2(d)) [48]. From Fig. 2(e), it can be concluded that the main component of the product is carbon, which is also mixed with iron balls that have not been completely removed. Iron balls play a catalytic role in the graphitization of carbon atoms [34]. The catalytic graphitization behavior of iron carbon alloy and the elemental composition of each part can be seen from the HAADF-STEM image of Nano-G and the corresponding energy-dispersive spectroscopy (EDS) maps from Fig. 2(e). To further quantify the structural differences between Nano-G and AG, pore size distribution and specific surface area were tested using the BET method (Fig. S9 in the ESM). The specific surface area of Nano-G was 45.7 $m^2 \cdot g^{-1}$, which is distinctly larger than that of AG (2.56 $m^2 \cdot g^{-1}$), and the proportion of mesopores in Nano-G is much higher than that in AG.

To investigate the electrochemical properties of Nano-G anode materials, the CR2016 half cells were assembled using potassium metal as the counter electrode. The mass ratio of the active material to binder is 9:1 and no conductive agent was added. More details can be seen in the experimental section. Long-term cycling tests were conducted to investigate the potassium storage capacity of Nano-G and AG at the small current density of 150 $mA \cdot g^{-1}$. And each cell was activated by two cycles at a current density of 30 $mA \cdot g^{-1}$ before long-term cycling. The loading mass of the electrode prepared by Nano-G and AG are 1.18 and 1.28 $mg \cdot cm^{-2}$ respectively. As can be seen in Fig. 3(a), the cell assembled with Nano-G still has a specific capacity of 247 $mAh \cdot g^{-1}$ at a current density of 150 $mA \cdot g^{-1}$ after 500 cycles, obviously higher than the cell assembled with AG whose specific capacity is 213 $mAh \cdot g^{-1}$ under the same condition. Moreover, the ICE of the half cell assembled by Nano-G can reach 81.0%, which is comparable to the ICE of AG. In addition, the initial capacity of the activation process of battery assembled with Nano-G is higher than that of AG. It is generally believed that the activation process is caused by the poor charge transfer kinetics of graphite electrodes and the large size of K^+ [49, 50]. Therefore, the Nano-G can effectively improve the charge transfer kinetic and facilitate the migration of K^+. Both MWCNTs and graphite shells in Nano-G can relieve the

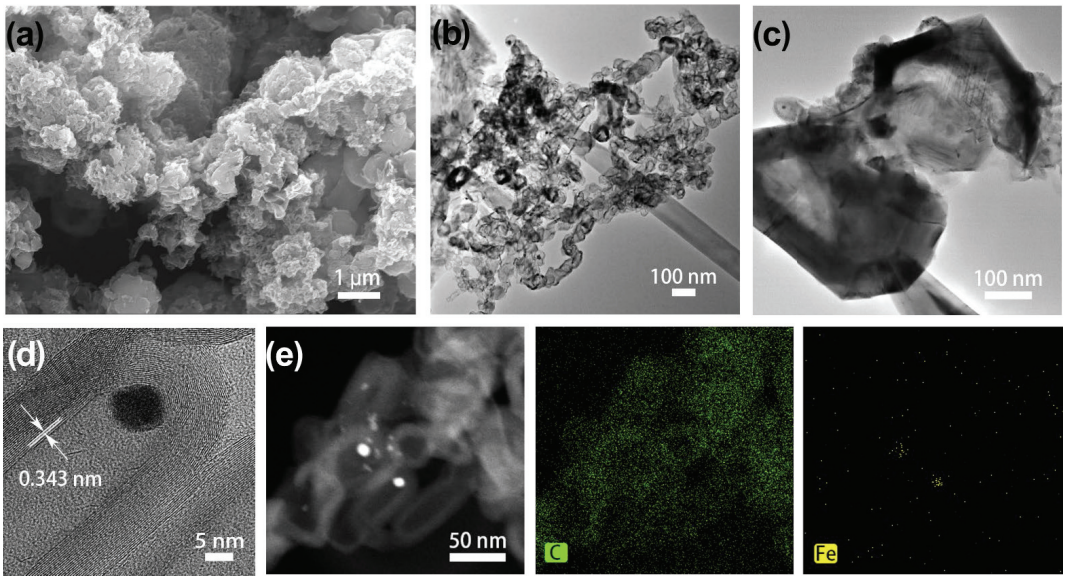

Figure 2 (a) SEM image of Nano-G. (b) TEM image of nanotubes. (c) TEM image of graphite shells. (d) HRTEM image, (e) HAADF-STEM image, and the corresponding EDS elemental mapping of Nano-G.

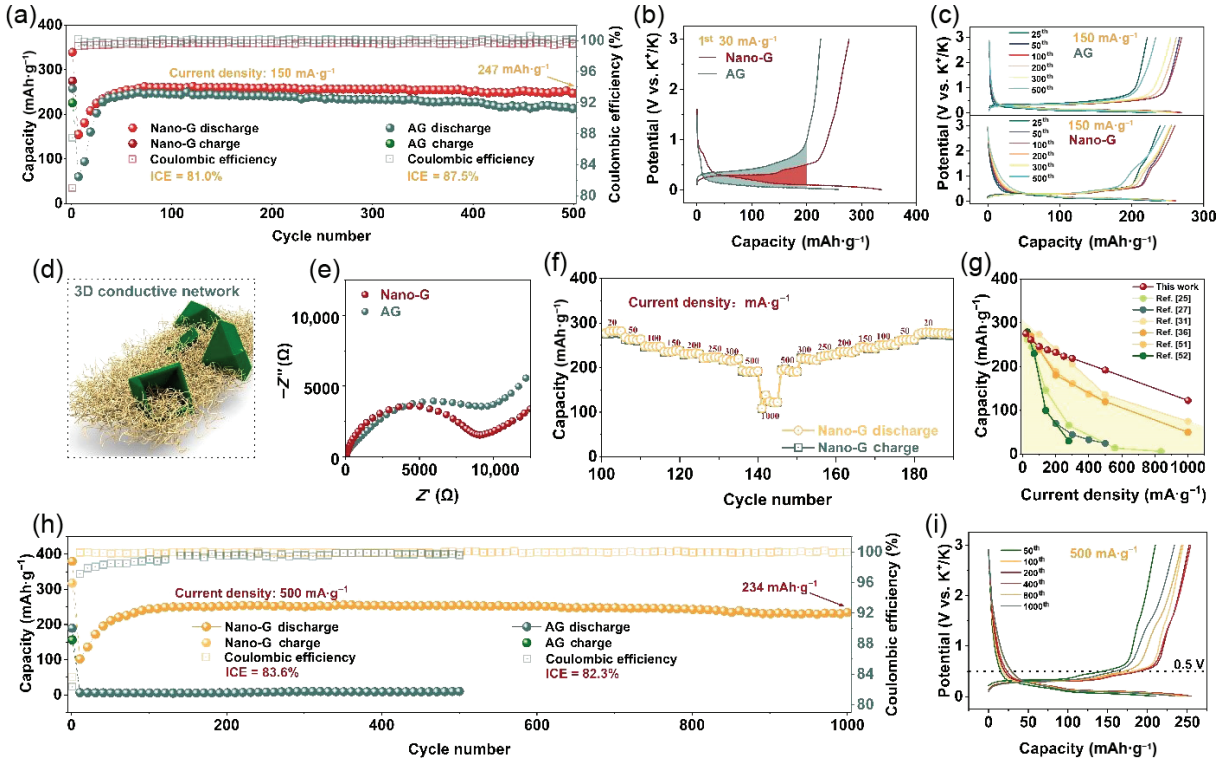

Figure 3 K-storage performances of the half cells. (a) Long-term cycling performance at 150 mA·g^{-1} after initial 2 cycles at 30 mA·g^{-1}. Galvanostatic charge/discharge profiles at (b) 30 mA·g^{-1} and (c) 150 mA·g^{-1} in potential window from 0.01 to 3.0 V. (d) Schematic diagram of 3D conductive network. (e) Nyquist plots of Nano-G and AG obtained before cycling. (f) Rate performance of Nano-G electrode and (g) comparison of the rate performances of Nano-G with other graphitic carbon materials reported in the literature. (h) Long-term cycling performance at 500 mA·g^{-1} after initial 2 cycles at 30 mA·g^{-1}. (i) Galvanostatic charge/discharge profiles at 500 mA·g^{-1} in potential window from 0.01 to 3.0 V.

volume expansion caused by the K^+, and their large specific surface area also ensures an effective contact between electrolyte and electrode, thereby shortening the migration path of K^+. Besides, the high graphitization degree of Nano-G also guarantees a high electronic conductivity and high ICE close to AG. The polarization of the both Nano-G and AG electrode can be clearly outlined from the charge/discharge profiles under 30 mA·g^{-1} (Fig. 3(b)). Even the current density is small as 30 mA·g^{-1}, the polarization of the electrode containing Nano-G is still significantly smaller than that of the AG. The significantly reduced polarization can effectively improve the rate performance of the half cell. From the charge/discharge platforms at different cycles at a current density of 150 mA·g^{-1} (Fig. 3(c)), it is clear that the polarization of the electrode containing Nano-G is smaller than that of the electrode containing AG, and its discharge platform remains low after 500 cycles while providing a better stability. So the 3D conductive structure composed of MWCNTs and graphite shells built by Nano-G is able to provide fast channels for electron and ion transport, and buffering the volume expansion caused by K^+ insertion (Fig. 3(d)).

The ion/electron transport properties of Nano-G compared with AG were further confirmed by the EIS test. Two semicircles with different charge-transfer resistance (R_{ct}) values before cycling were exhibited by the Nyquist plots of the samples. The R_{ct} value

of Nano-G is smaller than that of AG, which indicates that Nano-G has superior interface kinetics (Fig. 3(e)). The rate performance test was carried out on a half cell with a mass-loading of 1.49 mg·cm^{-1} after 2 cycles at a current density of 30 mA·g^{-1} and 98 cycles at a current density of 150 mA·g^{-1} respectively in order to exclude the influence of activation factors (Fig. S10 in the ESM). As can be seen from Fig. 3(d), even the current density is high as 1000 mA·g^{-1}, the specific capacity of Nano-G still reaches to 121 mAh·g^{-1}; and the specific capacity can recover to 267 mAh·g^{-1} when the current density restores to 20 mA·g^{-1} (Fig. 3(f)). Compared with the graphitic materials in other literatures, Nano-G displayed a better rate performance (Fig. 3(g)) [25, 27, 31, 36, 51, 52]. It is worthwhile to investigate the cycling ability of Nano-G under high current density. A half cell assembled by Nano-G with a mass loading of 1.08 mg·cm^{-2} was subjected to a long-term cycling test at a current density of 500 mA·g^{-1}. It achieved an ICE of 83.6% during the activation stage and still had a specific capacity of 234 mAh·g^{-1} after 1000 cycles. Under the same conditions, after the activation stage, the specific capacity of AG rapidly decayed to 9 mAh·g^{-1} due to large polarization (Fig. 3(h)), which proves the superiority of Nano-G in potassium storage at high current densities. Even the current density is as high as 500 mA·g^{-1}, the intercalation of K^+ does not occur in the form of shallow charging and discharging, and it can be concluded from the charge/discharge profiles that the discharge platform of Nano-G is very low, and most of the discharging capacity is occupied by the part where the potential is lower than 0.5 V (Fig. 3(i)), which indicates that the K^+ are deeply inserted. And the discharge platform remained unchanged after 1000 cycles, demonstrating that Nano-G is quite stable and capable of deep K^+ storage at high current densities. In order to further explore the structural stability of Nano-G, TEM and Raman analysis were performed on the cycled electrode. The TEM images of Nano-G after 1000 cycles (Fig. S11 in the ESM) show that although the material structure becomes loose, it is still rich in fine graphite structure which reflects the stability of the electrode material. And these fine graphite structures are interconnected, proving that the material can maintain high electronic conductivity even after multiple cycles. And the Raman spectroscopy result (Fig. S12 in the ESM) shows that the cycled material still retains the obvious Raman spectrum characteristics of graphite, which proves the stability of its chemical composition.

The Nano-G was assembled into PIBs anode and tested by CV measurements in a voltage window of 0.01–3 V (V vs. K^+/K) to evaluate its electrochemical performance. As shown in Fig. 4(a), three pairs of peaks (C_1/A_1, C_2/A_2, and C_3/A_3) which are associated with diffusion-controlled Faradaic processes can be seen. The curve shapes are similar with that of carbon nanotubes and graphitic carbon nanocages which have been observed before [32, 37], so it suggests that Nano-G has few-layered graphitic structure. The process of the irreversible decomposition of electrolyte to from solid electrolyte interphase (SEI) can be reflected by the weak cathodic peak located at 0.94 V which only appears in the 1st cycle. In the second and third cycles, the CV curves are overlapped which indicate the reversibility of Nano-G. The positions of cathodic peaks shift to the lower potentials and the anodic peaks shift to the higher potentials with increasing scan rates from 0.1 to 1.0 mV·s^{-1} (Fig. 4(b)), and it confirms that the three peaks are all from the Faradaic reactions of diffusion-limited. The *b* values were calculated by the relation between logarithms of peak currents and scan rates according to Eq. (1) [53]

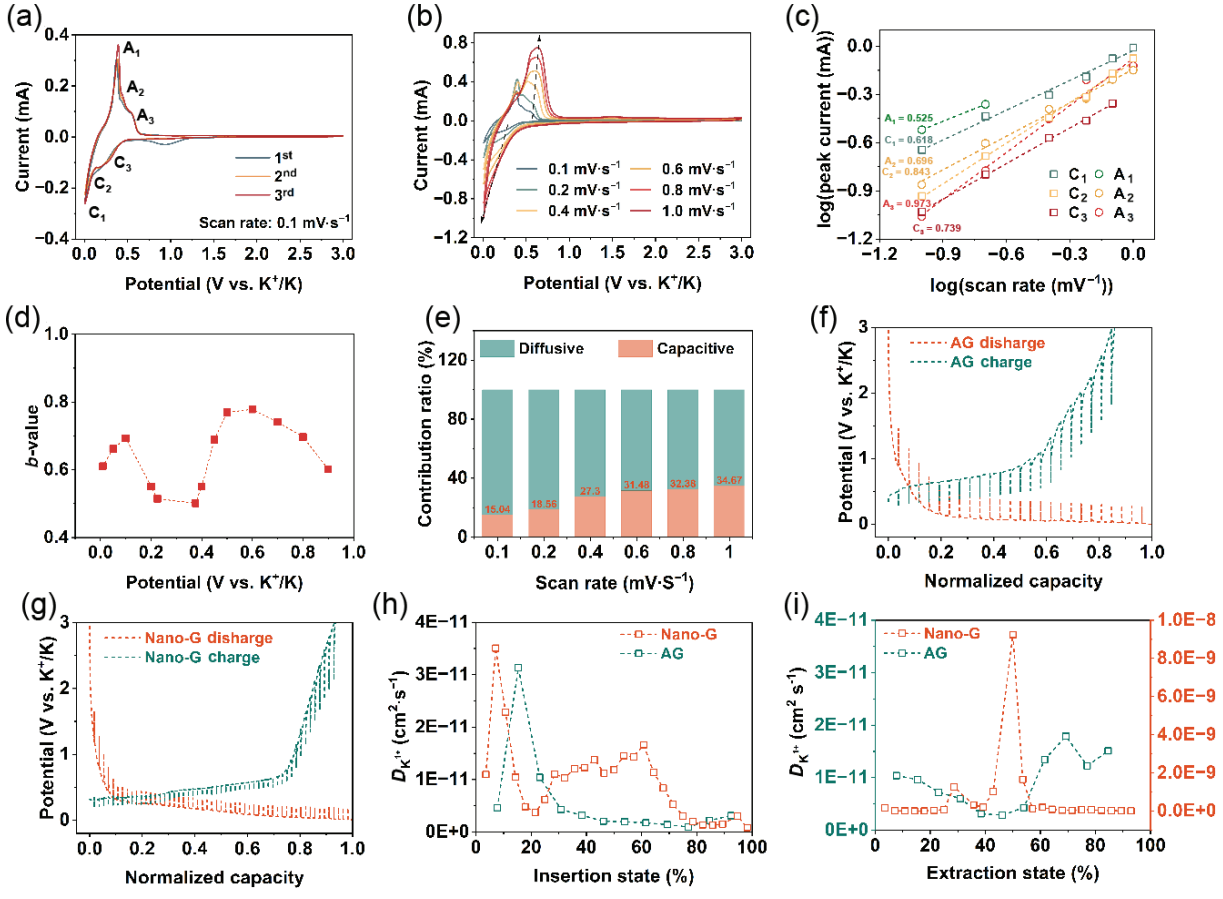

Figure 4 Kinetics analysis of K-storage. (a) CV curves of Nano-G at a scan rate of 0.1 mV·s^{-1} and (b) at various scan rates. (c) The logarithm relationship between the scan rates and the peak current densities. (d) Calculated *b* values of Nano-G for cathodic sweep. (e) Contribution of the surface-controlled process in Nano-G at different scan rates. GITT potential profiles of (f) AG and (g) Nano-G. K^+ diffusion coefficient as a function of the state of (h) the discharging process and (i) the charging process.

$$i = av^b \quad (1)$$

where the i and v represent current and scan rate respectively, both the a and b are adjustable parameters. As shown in Fig. 4(c), the results manifest the high b values about 0.739 and 0.973 of the C_3 and A_3 peaks separately, which indicate the fast Faradaic processes. The relatively low b values of 0.618/0.525 and 0.843/0.695 of the C_1/A_1 peaks and the C_2/A_2 peaks indicate a diffusion-controlled Faradaic behavior. The diffusion-controlled characteristic of the C_1/A_1 peaks and the C_2/A_2 peaks indicate that the K^+ storage occurs in low-potential range. After comparing the multi-sweep CV of graphitic nanocages and nanowires [32, 37], it can be found that the A_2/C_2 and the A_3/C_3 peaks are attributed to the different structures and morphologies between MWCNTs and graphite shells, and the A_1/C_1 peaks are correspond to the deep insertion of K^+.

The b values at 0.01–0.9 V for the cathodic sweep of Nano-G are calculated. It can be seen in Fig. 4(d) that the b values fluctuate under 0.8, and from 0.4 to 0.1 V, the b values of Nano-G are lower than 0.6, indicating the capacity is mainly controlled by diffusion at this stage. The current response at a certain potential is usually divided into the capacitive process of surface-dominated (k_1v) and intercalation process of diffusion-controlled ($k_2v^{1/2}$) according to Eq. (2)

$$i(V) = k_1v + k_2v^{1/2} \quad (2)$$

The green region and orange region in Fig. 4(e) represent the current provided by the process of intercalation and capacitance respectively. The ratio of the current provided by surface-dominated capacitive process increases as the scan rates increase, and the growth rate slows down when the scan rate is greater than 0.4 mV·s^{-1} (Fig. 4(e)).

The GITT test was used to further understand the kinetic processes by determine the K^+ diffusion coefficients (D_K). Figures 4(f) and 4(g) show the potential curves at a pulse current of 35 mA·g^{-1} for 10 min and relax for 30 min in potential window of 0.01–3 V. The potential changes during each relaxation period of Nano-G are smaller and its pulse counts are more than AG, which indicates the better kinetic property of Nano-G. The D_K values are calculated by Eq. (3)

$$D_K = \frac{4}{\pi\tau}\left(\frac{m_B V_M}{M_B S}\right)^2\left(\frac{\Delta E_S}{\Delta E_\tau}\right)^2 \quad (3)$$

The τ, m_B, and S represent the duration of the current pulse, the electrode active material mass, and the geometric area of the electrode separately; and ΔE_S, ΔE_τ, V_M, and M_B represent the quasi-thermodynamic equilibrium potential difference before and after the current pulse, the potential difference during current pulse, the molar volume of the Nano-G, and the molar mass of carbon respectively. The calculated D_K values during the discharging process can be seen in Fig. 4(h). The higher D_K of Nano-G than AG indicates the faster K^+ diffusion of Nano-G, especially in 25%–75% of the insertion state. Besides, the calculated D_K values during the charging process are also shown in Fig. 4(i). It is obvious that when the extraction state is between 30% and 60%, the D_K value of Nano-G is much higher in the order of 10^{-9} than that of AG in the order of 10^{-12}, which further verifies the fast kinetic process of K^+ during the charging process. The above results of CV and GITT show that the Nano-G material can achieve diffusion-controlled graphite potassium storage behavior with the help of high ion diffusion kinetics.

The *in situ* XRD test of the Nano-G was carried out to probe its potassium storage mechanism (Fig. 5(a)). A self-made stainless steel *in situ* mold with a window was used as the battery shell for *in situ* testing. The beryllium and quartz sheets were used as packaging windows for *in situ* XRD and *in situ* Raman testing, respectively. Electrode sheets are prepared by mixing Nano-G with polytetrafluoroethylene (PTFE) at a mass ratio of 9:1. After rolling and cutting, the above mixture was made into electrode sheets with a mass about 5 mg and an area about 0.8 cm^{-2} for *in situ* testing. The current density used for the charge/discharge test was 150 mA·g^{-1} and the other parameters are consistent with that of the half cells.

It can be found that the graphite peak disappeared during the discharge process, and the KC_{36} and KC_{24} complexes were gradually formed. After the K^+ was completely extracted, the electrode material returned to the graphite phase, indicating the reversibility of the material and the charge–discharge behavior of typical graphite [43, 54], which also explained the reason of its low discharge platform. *In situ* Raman analysis on the material was also carried out and found that the D and 2D peaks of the material disappear during discharge (after K^+ insertion) around 0.4 V, and regenerate when K^+ is extracted around 0.7 V, this also proves that the properties of graphite are accompanied by the potassium storage process of the Nano-G electrode (Figs. 5(b)–5(d)) [36, 55].

To evaluate the commercial application prospect of the Nano-G anode, the full cells using commercialized PTCDA as the cathode and 3 M KFSI dissolved in DME solution as the electrolyte was assembled and tested, details can be seen in experimental section. The PTCDA and Nano-G were both pre-cycled. The pre-cycle curve of PTCDA half cell can be seen in Fig. S13 in the ESM. The charge/discharge curves of the PTCDA cathode, the Nano-G anode half cells, and the full cell are shown in Fig. 6(a). The normalized capacity is calculated by dividing the capacity corresponding to each voltage point by the total capacity and it is used as the x-axis. From the diagram, it can be seen that the discharge platform of the matched full cell is about 2.2 V close to that of the PTCDA in the half cell, which is caused by the low and

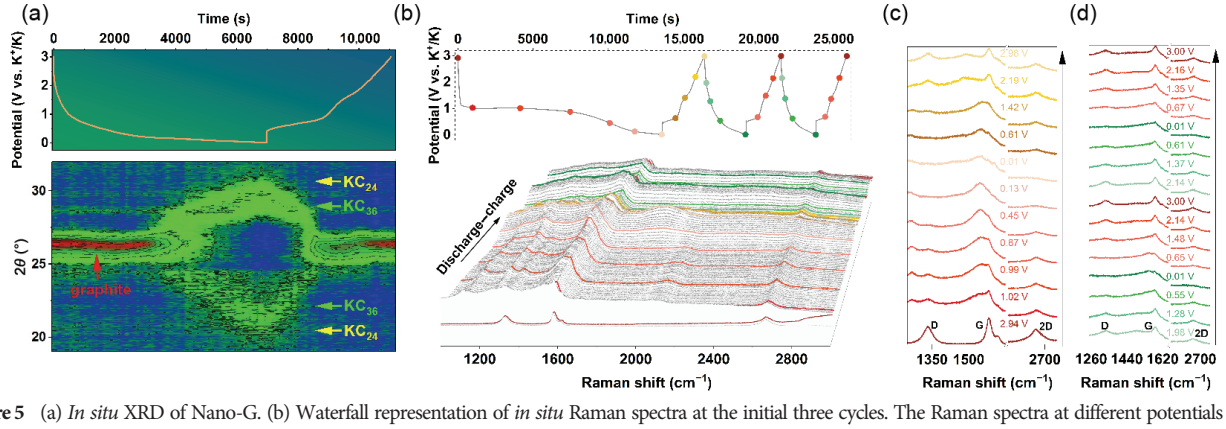

Figure 5 (a) *In situ* XRD of Nano-G. (b) Waterfall representation of *in situ* Raman spectra at the initial three cycles. The Raman spectra at different potentials in (c) the first cycle and (d) the second and third cycles.

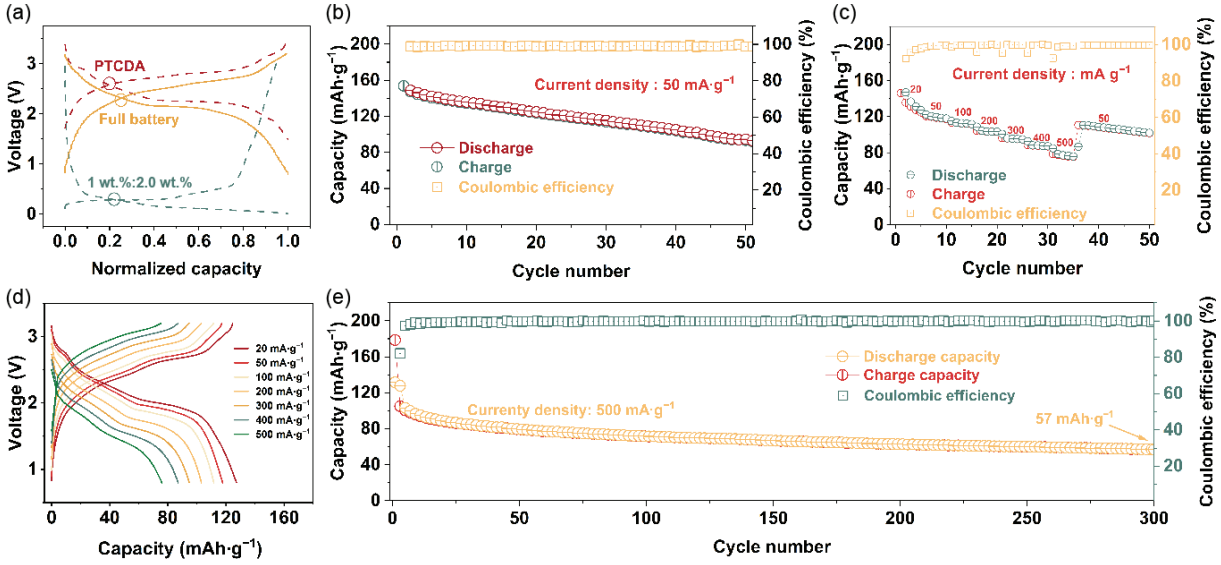

Figure 6 Electrochemical performance of the full cells. (a) Normalized charge/discharge profiles of half and full cells. (b) Cycling performances of the Nano-G||PTCDA cell at a current density of 50 mA·g^{-1}. (c) Rate performance of the full battery. (d) Charge/discharge voltage profiles of the full battery at different current densities. (e) Cycling performances of the Nano-G||PTCDA cell at a current density of 500 mA·g^{-1}.

flat discharge platform of the Nano-G anode and further indicates the suitability of Nano-G as an anode for assembling high voltage PIBs. Compared to amorphous carbon materials, Nano-G can increase the output voltage and thus the energy density [56]. The full battery still has a specific capacity of 94 mAh·g^{-1} at a current density of 50 mA·g^{-1} after 50 cycles at the anode capacity/cathode capacity (*N*/*P*) ratio of 1.2, calculated based on the mass of the active material of cathode (Fig. 6(b)). By conducting rate performance tests on the full cell, it can be found that the full cell still maintains a specific capacity of 78.5 mAh·g^{-1} at a current density of 500 mA·g^{-1}. When the current density recovers to 50 mA·g^{-1}, it can recover to a specific capacity of 110 mAh·g^{-1} (Fig. 6(c)). When the current density increases, it can maintain high specific capacities and appropriate discharge platforms under large polarization (Fig. 6(d)). The full battery also underwent long cycle at a current density of 500 mA·g^{-1} and it still displayed a specific capacity of 57 mAh·g^{-1} after 300 cycles (Fig. 6(e)), which means a good cycling stability of Nano-G anode.

4 Conclusion

In summary, a novel nanostructured graphite material (Nano-G) was synthesized and the low-temperature catalytic graphitization effect of MIL-100 (Fe) on carbon sources was systematically investigated. Compared to commercial AG anode obtained at 2800 °C, the Nano-G can form at 1100 °C and be gifted with a unique structure. Moreover, the high degree of graphitization can guarantee a high ICE as that of AG. The 3D conductive network built by MWCNTs and graphite shells can provide fast channels for electron and K^+ transport, while buffering the volume expansion caused by the insertion/extraction of K^+. Electrochemical tests proved that the Nano-G used as the anode of PIBs can achieve an ICE of 83.6% and a specific capacity of 234 mAh·g^{-1} after 1000 cycles at a current density of 500 mA·g^{-1}. Meanwhile, the low electrode polarization and potassium storage mechanism of Nano-G anode were demonstrated and its application potential was also proved by integrating with PTCDA cathode in PIBs full cells. The unique structure of Nano-G also paves the way for inexpensive iron-based MOF materials as carriers to catalyze the graphitization of renewable carbon sources. And the low-temperature pyrolysis preparation of graphite anode materials can further reduce production costs and assist PIBs for using in large-scale EESs.

Acknowledgements

The authors greatly appreciate the financial support from the National Key Research and Development Program of China (Nos. 2022YFB2404300 and 2023YFB3809303), the National Natural Science Foundation of China (Nos. 51832004 and 52127816), and State Key Laboratory of Advanced Technology for Materials Synthesis and Processing (No. WUT: 2022-KF-4).

Electronic Supplementary Material: Supplementary material (SEM and XRD images, TG and BET measurements, TEM images, and Raman spectroscopy measurements) is available in the online version of this article at https://doi.org/10.1007/s12274-024-6429-4.

References

[1] Fan, Q. Z.; Lin, L.; Jian, Z. L.; Liu, G. M.; Zhao, C. X.; Qi, Y. Y. Biomass-derived carbon fibers modified by Ag/rGO for high-performance Li metal composite anode. *J. Mater. Sci. Mater. Electron.* **2023**, *34*, 25.

[2] Li, G. L.; Wang, Y. T.; Guo, H.; Liu, Z. L.; Chen, P. H.; Zheng, X. Y.; Sun, J. L.; Chen, H.; Zheng, J.; Li, X. G. Direct plasma phosphorization of Cu foam for Li ion batteries. *J. Mater. Chem. A* **2020**, *8*, 16920–16925.

[3] Abdelmaoula, A. E.; Du, L. L.; Xu, L.; Cheng, Y.; Mahdy, A. A.; Tahir, M.; Liu, Z. A.; Mai, L. Biomimetic brain-like nanostructures for solid polymer electrolytes with fast ion transport. *Sci. China Mater.* **2022**, *65*, 1476–1484.

[4] Su, L.; Ren, J. K.; Lu, T.; Chen, K. X.; Ouyang, J. W.; Zhang, Y.; Zhu, X. Y.; Wang, L. Y.; Min, H. H.; Luo, W. et al. Deciphering structural origins of highly reversible lithium storage in high entropy oxides with *in situ* transmission electron microscopy. *Adv. Mater.* **2023**, *35*, 2205751.

[5] Guerra, O. J. Beyond short-duration energy storage. *Nat. Energy* **2021**, *6*, 460–461.

[6] Pomerantseva, E.; Bonaccorso, F.; Feng, X. L.; Cui, Y.; Gogotsi, Y. Energy storage: The future enabled by nanomaterials. *Science* **2019**, *366*, eaan8285.

[7] Zhang, X.; Meng, J. S.; Wang, X. P.; Xiao, Z. T.; Wu, P. J.; Mai, L. Comprehensive insights into electrolytes and solid electrolyte interfaces in potassium-ion batteries. *Energy Storage Mater.* **2021**, *38*, 30–49.

[8] Tarascon, J. M. Is lithium the new gold. *Nat. Chem.* **2010**, *2*, 510–510.

[9] Komaba, S.; Hasegawa, T.; Dahbi, M.; Kubota, K. Potassium

intercalation into graphite to realize high-voltage/high-power potassium-ion batteries and potassium-ion capacitors. *Electrochem. Commun.* **2015**, *60*, 172–175.
[10] Hosaka, T.; Kubota, K.; Kojima, H.; Komaba, S. Highly concentrated electrolyte solutions for 4 V class potassium-ion batteries. *Chem. Commun.* **2018**, *54*, 8387–8390.
[11] Asher, R. C.; Wilson, S. A. Lamellar compound of sodium with graphite. *Nature* **1958**, *181*, 409–410.
[12] Ge, P.; Fouletier, M. Electrochemical intercalation of sodium in graphite. *Solid State Ionics* **1988**, *28–30*, 1172–1175
[13] Wen, Y.; He, K.; Zhu, Y. J.; Han, F. D.; Xu, Y. H.; Matsuda, I.; Ishii, Y.; Cumings, J.; Wang, C. S. Expanded graphite as superior anode for sodium-ion batteries. *Nat. Commun.* **2014**, *5*, 4033.
[14] Luo, W.; Li, F.; Zhang, W. R.; Han, K.; Gaumet, J. J.; Schaefer, H. E.; Mai, L. Encapsulating segment-like antimony nanorod in hollow carbon tube as long-lifespan, high-rate anodes for rechargeable K-ion batteries. *Nano Res.* **2019**, *12*, 1025–1031.
[15] Wang, C. X.; Yu, R. H.; Luo, W.; Feng, W. C.; Shen, Y. H.; Xu, N.; Mai, L. Chemical cross-linking and mechanically reinforced carbon network constructed by graphene boosts potassium ion storage. *Nano Res.* **2022**, *15*, 9019–9025.
[16] Feng, Y. H.; Rao, A. M.; Zhou, J.; Lu, B. A. Selective potassium deposition enables dendrite-resistant anodes for ultrastable potassium-metal batteries. *Adv. Mater.* **2023**, *35*, 2300886.
[17] Hu, Y.; Tang, C.; Lv, F. T.; Du, A. J.; Wu, Z. S.; Zhang, H. J. K-functionalized carbon quantum dots-induced interface assembly of carbon nanocages for ultrastable potassium storage performance. *Small Methods* **2022**, *6*, 2101627.
[18] Xiong, P. X.; Zhao, X. X.; Xu, Y. H. Nitrogen-doped carbon nanotubes derived from metal-organic frameworks for potassium-ion battery anodes. *ChemSusChem* **2018**, *11*, 202–208.
[19] Wang, M.; Wang, Q. C.; Ding, X. Y.; Wang, Y. S.; Xin, Y. H.; Singh, P.; Wu, F.; Gao, H. C. The prospect and challenges of sodium-ion batteries for low-temperature conditions. *Interdiscip. Mater.* **2022**, *1*, 373–395.
[20] Wang, H.; Liu, F.; Yu, R. H.; Wu, J. S. Unraveling the reaction mechanisms of electrode materials for sodium-ion and potassium-ion batteries by *in situ* transmission electron microscopy. *Interdiscip. Mater.* **2022**, *1*, 196–212.
[21] Deng, L. Q.; Qu, J. L.; Niu, X. G.; Liu, J. Z.; Zhang, J.; Hong, Y. R.; Feng, M. Y.; Wang, J. W.; Hu, M.; Zeng, L. et al. Defect-free potassium manganese hexacyanoferrate cathode material for high-performance potassium-ion batteries. *Nat. Commun.* **2021**, *12*, 2167.
[22] Bie, X. F.; Kubota, K.; Hosaka, T.; Chihara, K.; Komaba, S. A novel K-ion battery: Hexacyanoferrate(II)/graphite cell. *J. Mater. Chem. A* **2017**, *5*, 4325–4330.
[23] Li, X. D.; Li, J. L.; Ma, L.; Yu, C. Y.; Ji, Z.; Pan, L. K.; Mai, W. Graphite anode for potassium ion batteries: Current status and perspective. *Energy Environ. Mater.* **2022**, *5*, 458–469.
[24] Wall Street Crocodile. SOHU: Top 10 shipments of anode materials in China in 2023H1 (in Chinese) [Online]. https://www.sohu.com/a/715607072_121123888 (accessed Nov 1, 2023).
[25] Kim, J. K.; Jung, D. S.; Lee, J. K.; Kang, Y. C. Less energy-intensive synthesis of mesoporous multi-oriented graphite microspheres with low defect concentration for advanced potassium-ion battery anodes. *Chem. Eng. J.* **2022**, *443*, 136545.
[26] Lee, S. M.; Kang, D. S.; Roh, J. S. Bulk graphite: Materials and manufacturing process. *Carbon Lett.* **2015**, *16*, 135–146.
[27] Choi, S. H.; Baucom, J.; Li, X. R.; Shen, L.; Seong, Y. H.; Han, I. S.; Choi, Y. J.; Ko, Y. N.; Kim, H. J.; Lu, Y. F. Porous carbon microspheres with highly graphitized structure for potassium-ion storage. *J. Colloid Interface Sci.* **2020**, *577*, 48–53.
[28] Shen, M. K.; Ding, H. B.; Fan, L.; Rao, A. M.; Zhou, J.; Lu, B. A. Neuromorphic carbon for fast and durable potassium storage. *Adv. Funct. Mater.* **2023**, *33*, 2213362.
[29] Tian, S.; Jiang, Q. T.; Cai, T. H.; Wang, Y. S.; Wang, D. D.; Kong, D. Q.; Ren, H.; Zhou, J.; Xing, W. Graphitized electrospun carbon fibers with superior cyclability as a free-standing anode of potassium-ion batteries. *J. Power Sources* **2020**, *474*, 228479.
[30] Ma, X. M.; Fu, H. W.; Shen, J. Y.; Zhang, D. W.; Zhou, J. W.; Tong, C. Y.; Rao, A. M.; Zhou, J.; Fan, L.; Lu, B. A. Green ether electrolytes for sustainable high-voltage potassium ion batteries. *Angew. Chem., Int. Ed.* **2023**, *62*, e202312973.
[31] Li, Z. Q.; Wen, J. Q.; Cai, Y. Q.; Lv, F. T.; Zeng, X.; Liu, Q.; Masese, T.; Zhang, C. X.; Yang, X. S.; Ma, Y. W. et al. Hydrated Bi-Ti-bimetal ethylene glycol: A new high-capacity and stable anode material for potassium-ion batteries. *Adv. Funct. Mater.* **2023**, *33*, 2300582.
[32] Sun, D. G.; Tang, C.; Cheng, H.; Xu, W. L.; Du, A. J.; Zhang, H. J. Pumpkin-like MoP-MoS_2@aspergillus niger spore-derived N-doped carbon heterostructure for enhanced potassium storage. *J. Energy Chem.* **2022**, *72*, 479–486.
[33] He, T.; Kong, X. J.; Li, J. R. Chemically stable metal-organic frameworks: Rational construction and application expansion. *Acc. Chem. Res.* **2021**, *54*, 3083–3094.
[34] Hunter, R. D.; Ramírez-Rico, J.; Schnepp, Z. Iron-catalyzed graphitization for the synthesis of nanostructured graphitic carbons. *J. Mater. Chem. A* **2022**, *10*, 4489–4516.
[35] Luo, W.; Wan, J. Y.; Ozdemir, B.; Bao, W. Z.; Chen, Y. N.; Dai, J. Q.; Lin, H.; Xu, Y.; Gu, F.; Barone, V. et al. Potassium ion batteries with graphitic materials. *Nano Lett.* **2015**, *15*, 7671–7677.
[36] Zhang, W. L.; Ming, J.; Zhao, W. L.; Dong, X. C.; Hedhili, M. N.; Costa, P. M. F. J.; Alshareef, H. N. Graphitic nanocarbon with engineered defects for high-performance potassium-ion battery anodes. *Adv. Funct. Mater.* **2019**, *29*, 1903641.
[37] Cao, B.; Zhang, Q.; Liu, H.; Xu, B.; Zhang, S. L.; Zhou, T. F.; Mao, J. F.; Pang, W. K.; Guo, Z. P.; Li, A. et al. Graphitic carbon nanocage as a stable and high power anode for potassium-ion batteries. *Adv. Energy Mater.* **2018**, *8*, 1801149.
[38] Zhao, C. B.; Jiang, Z.; Liu, Y.; Zhou, Y.; Yin, P. C.; Ke, Y. B.; Deng, H. X. Molecular compartments created in metal-organic frameworks for efficient visible-light-driven CO_2 overall conversion. *J. Am. Chem. Soc.* **2022**, *144*, 23560–23571.
[39] Horcajada, P.; Surblé, S.; Serre, C.; Hong, D. Y.; Seo, Y. K.; Chang, J. S.; Greneche, J. M.; Margiolaki, I.; Férey, G. Synthesis and catalytic properties of MIL-100(Fe), an iron(III) carboxylate with large pores. *Chem. Commun.* **2007**, 2820–2822
[40] Liu, Y.; Dai, H. D.; Wu, L.; Zhou, W. B.; He, L.; Wang, W. G.; Yan, W. Q.; Huang, Q. H.; Fu, L. J.; Wu, Y. P. A large scalable and low-cost sulfur/nitrogen dual-doped hard carbon as the negative electrode material for high-performance potassium-ion batteries. *Adv. Energy Mater.* **2019**, *9*, 1901379.
[41] Feng, W. C.; Wang, H.; Jiang, Y. L.; Zhang, H. Z.; Luo, W.; Chen, W.; Shen, C. L.; Wang, C. X.; Wu, J. S.; Mai, L. Q. A strain-relaxation red phosphorus freestanding anode for non-aqueous potassium ion batteries. *Adv. Energy Mater.* **2022**, *12*, 2103343.
[42] Jian, Z. L.; Luo, W.; Ji, X. L. Carbon electrodes for K-ion batteries. *J. Am. Chem. Soc.* **2015**, *137*, 11566–11569.
[43] Liu, Y.; Lu, Y. X.; Xu, Y. S.; Meng, Q. S.; Gao, J. C.; Sun, Y. G.; Hu, Y. S.; Chang, B. B.; Liu, C. T.; Cao, A. M. Pitch-derived soft carbon as stable anode material for potassium ion batteries. *Adv. Mater.* **2020**, *32*, 2000505.
[44] Sadezky, A.; Muckenhuber, H.; Grothe, H.; Niessner, R.; Pöschl, U. Raman microspectroscopy of soot and related carbonaceous materials: Spectral analysis and structural information. *Carbon* **2005**, *43*, 1731–1742.
[45] Shin, M. C.; Kim, J. H.; Nam, S.; Oh, Y. J.; Jin, H. J.; Park, C. R.; Zhang, Q.; Yang, S. J. Atomic-distributed coordination state of metal-phenolic compounds enabled low temperature graphitization for high-performance multioriented graphite anode. *Small* **2020**, *16*, 2003104.
[46] Gomez-Martin, A.; Martinez-Fernandez, J.; Ruttert, M.; Heckmann, A.; Winter, M.; Placke, T.; Ramirez-Rico, J. Iron-catalyzed graphitic carbon materials from biomass resources as anodes for lithium-ion batteries. *ChemSusChem* **2018**, *11*, 2776–2787.
[47] Kwiecinska, B.; Murchison, D. G.; Scott, E. Optical properties of graphite. *J. Microsc.* **1977**, *109*, 289–302.
[48] Malard, L. M.; Pimenta, M. A.; Dresselhaus, G.; Dresselhaus, M. S. Raman spectroscopy in graphene. *Phys. Rep.* **2009**, *473*, 51–87.
[49] Wang, D. D.; Li, L. J.; Zhang, Z. H.; Liu, J.; Guo, X. S.; Mao, C. M.; Peng, H. R.; Li, Z. J.; Li, G. C. Mechanistic insights into the intercalation and interfacial chemistry of mesocarbon microbeads anode for potassium ion batteries. *Small* **2021**, *17*, 2103557.

[50] Li, W. D.; Wang, D. Z.; Gong, Z. J.; Yin, Z. M.; Guo, X. S.; Liu, J.; Mao, C. M.; Zhang, Z. H.; Li, G. C. A robust strategy for engineering Fe_7S_8/C hybrid nanocages reinforced by defect-rich MoS_2 nanosheets for superior potassium-ion storage. *ACS Nano* **2020**, *14*, 16046–16056.

[51] Feng, Y. H.; Chen, S. H.; Shen, D. Y.; Zhou, J.; Lu, B. A. Cross-linked hollow graphitic carbon as low-cost and high-performance anode for potassium ion batteries. *Energy Environ. Mater.* **2021**, *4*, 451–457.

[52] Wang, D. N.; Du, X. Q.; Zhang, B. Solvent molecular design to regulate the intercalation behavior in ether electrolyte for stable graphite anodes in potassium-ion batteries. *Small Struct.* **2022**, *3*, 2200078.

[53] Brezesinski, T.; Wang, J.; Tolbert, S. H.; Dunn, B. Ordered mesoporous α-MoO_3 with iso-oriented nanocrystalline walls for thin-film pseudocapacitors. *Nat. Mater.* **2010**, *9*, 146–151.

[54] Fan, L.; Ma, R. F.; Zhang, Q. F.; Jia, X. X.; Lu, B. A. Graphite anode for a potassium-ion battery with unprecedented performance. *Angew. Chem., Int. Ed.* **2019**, *58*, 10500–10505.

[55] Share, K.; Cohn, A. P.; Carter, R.; Rogers, B.; Pint, C. L. Role of nitrogen-doped graphene for improved high-capacity potassium ion battery anodes. *ACS Nano* **2016**, *10*, 9738–9744.

[56] Tan, W.; Wang, L. N.; Liu, K.; Lu, Z. G.; Yang, F.; Luo, G. F.; Xu, Z. H. Bitumen-derived onion-like soft carbon as high-performance potassium-ion battery anode. *Small* **2022**, *18*, 2203494.